Vol.67: e24230818, 2024
https://doi.org/10.1590/1678-4324-2024230818
ISSN 1678-4324 Online Edition

BABT
Brazilian Archives of Biology and Technology

Article - Engineering, Technology and Techniques

Multi-Period Optimal Power Flow for Smart Transformer-based Meshed Hybrid AC/DC Microgrids

Rafael Augusto Núñez Rodríguez[1,2*]
https://orcid.org/0000-0001-6775-776X

Clodomiro Unsihuay-Vila[3]
https://orcid.org/0000-0002-1639-7765

Johnny Posada Contreras[4]
https://orcid.org/0000-0001-7576-1021

Omar Pinzon Ardila[5]
https://orcid.org/0000-0001-8765-1479

[1]Universidad Autónoma de Bucaramanga, Facultad de Ingeniería, Bucaramanga, Colombia; [2]Unidades Tecnológicas de Santander, Programa de Ingeniería Electrónica, Bucaramanga, Colombia; [3]Universidade Federal do Paraná (UFPR), Departamento de Engenharia Elétrica, Curitiba, Brasil; [4]Universidad Autónoma de Occidente, Facultad de Ingeniería, Cali, Colombia; [5]Universidad Pontificia Bolivariana, Facultad de Ingeniería Eléctrica y Electrónica, Bucaramanga, Colombia.

Editor-in-Chief: Alexandre Rasi Aoki
Associate Editor: Alexandre Rasi Aoki

Received: 03-Aug-2023; Accepted: 30-Nov-2023

*Correspondence: rnunez281@unab.edu.co; Tel.: +57 301 5467127 (R.A.R.N.).

HIGHLIGHTS

- Impact analysis of Smart Transformer-based Meshed Hybrid AC/DC Microgrids with high penetration of distributed energy resources.
- Formulation of a Multi-Period Optimal Power Flow model to minimize operating cost, voltage deviation and losses in a hybrid AC/DC microgrid.
- Computational model for Day-Ahead Optimal Operation Planning of Inverter-based resources such as photovoltaic generators, energy storage systems and Smart Transformers.

Abstract: Smart Transformer (ST)-based Meshed Hybrid AC/DC Microgrids (MHM) present advantages concerning the performance of conventional AC/DC microgrids (MG). Despite this, MHMs present challenges in managing and controlling electronic converters associated with the ST and Distributed Energy Resources (DER), a scenario that makes it complex to achieve optimal system performance. Additionally, the high penetration of DER would impact the voltage profile, reduce the reactive compensation, and increase the losses in the distribution lines at a high cost in operation. This work proposes an optimal power management computational model for the day-ahead optimal operation planning of ST-based MHM. The management algorithm delivers the optimal operating points of each of the converters of the MG so that it allows the control of active power on both the AC and DC sides; likewise, it will enable reactive power injection control according to the availability of the solar photovoltaic resource and Battery Energy Storage Systems (BESS). According to the tests performed under different operation scenarios with varying degrees of penetration of Photovoltaic Generator (PVG), the benefits of implementing the ST as an energy router according to the operating set

points by the optimization algorithm are evidenced. Integrating the ST in MHM and optimization algorithms is a suitable alternative for managing microgrids with high penetration of distributed energy resources. This allows for improving the voltage profile in the MHM, reducing losses in the lines and energy exchange costs with the distribution network.

Keywords: Day-Ahead Optimal Operation Planning; Smart Transformer; Meshed Hybrid Microgrids; Energy Management; Distributed Energy Resources; Multi-period OPF.

INTRODUCTION

In line with the need to reduce greenhouse gas (GHG) emissions, it is necessary to promote technological development to increase electricity coverage, as well as integrate BESS (1) and DER [1][2][3]. MGs make the integration of DER on a scale into the Distribution System (DS) more flexible while improving the reliability and energy efficiency of the electrical grid [4]. AC MGs are widely used; however, despite the degree of maturity of control and management techniques, they present the need to introduce Distribution Generation (DG) synchronization and reactive power management schemes [5]. On the other hand, DC MGs allow the integration of DER and BESS with higher efficiency by using fewer converters and no reactive power. However, incorporating these elements into the common DC bus makes voltage control complex and power-sharing algorithms are necessary [6][7].

Hybrid AC/DC Microgrids (HMGs) appear as a typology of great interest since they combine the main advantages of AC and DC MGs [5][8][9], with a high degree of reliability, flexibility, and economy [10]. These MG configurations have been conventionally implemented based on radial distribution schemes with satisfactory results. However, they might show low reliability regarding power supply since DER can cause voltage increases and exceed the limit [8]. In contrast, high load demand can cause a significant voltage to decrease at the end of the line and, at the same time, overload distribution lines and connected transformers [11]. Therefore, voltage regulation is challenging, especially for long feeders, and may require voltage regulation devices [12][13]. Thus, in recent years, MHM [14] has been proposed as a feasible alternative to increase the penetration of DER and BESS [15]. Due to the degrees of freedom of the ST, it can be transformed into MHMs by interconnecting the Electronic Power Interface (EPI) of each DER with the ST stages at the DC or AC ports [14]. STs shape various energy flow paths and energy management strategies [14], in addition to eliminating the need for an Interlinking Converter (IC) [16].

Nonetheless, MHMs must integrate supervisory control coupled with an Energy Management System (EMS) to optimize network performance in terms of power quality, reduced line losses, and MG fault management capability [17]. Recently, EMS strategies have been proposed in MHM that integrate BESS and PVG in connection and disconnection maneuvers [18][19]. Similarly, they have shown that voltage and load profile control can be realized by meshing the network in a ring configuration with bidirectional power flow control [17], facilitating independent active and reactive power management [20]. Under this novel approach, the advancement and development of MHM require an EMS to optimize the performance of the network in terms of network voltage limit, overcurrent, and line losses, as well as to manage network operation in the event of failure, avoiding network collapse [17][21].

This work proposes an optimal power management computational model for the day-ahead optimal operation planning [22] of ST-based MHM. The management algorithm delivers the optimal operating points of each of the inverter-based resources of the MG so that it allows the control of active power on both the AC and DC sides; likewise, it will enable reactive power injection control according to the availability of the solar photovoltaic resource and BESS. A decoupled structure of the TS allows power flow control between the AC and DC side of the MHM since the third stage of the TS is considered an active Voltage-Sourced Converter (VSC) whose operating point is set by the optimization algorithm. Thus, the main contribution of this paper is the impact of ST-based MHM with high penetration of distributed energy resources based on a multi-objective multi-period problem to minimize operating cost, voltage deviation, losses in AC/DC microgrid, and VSC's optimal power dispatch.

This paper is organized as follows: the material and methods section presents the main mathematical formulation and data used in the proposed model, followed by the results section. The paper ends with the conclusion section.

MATERIAL AND METHODS

Some elements must be introduced to recognize the nature of the equations involved in the MHM's power transfer between the AC and DC sides and formulate the optimization problem. For this, the operating

principle of the VSC and the variables in the power flow equations between the VSC ports are discussed. On the other hand, the principle of operation of the ST as a multi-stage electronic converter with decoupled control loops, which are important features for formulating the power flow equations between the ST stages and MHM, is introduced. Finally, the relevant equations for developing the optimization problem and the constraints associated with each microgrid element are described on the AC or DC side.

Voltage-Sourced Converter

The DERs considered in this work operate in connected mode (AC or DC current source) on the AC and DC side through a VSC and bidirectional DC-DC converter. The VSC allows making active and reactive power control independently for both the PVG and the BESS on the AC side, while the bidirectional DC-DC converter does the same for active power control on the DC side; all this, according to the availability of the available resource of the PVG and the State of Charge (SoC) of the BESS during the day.

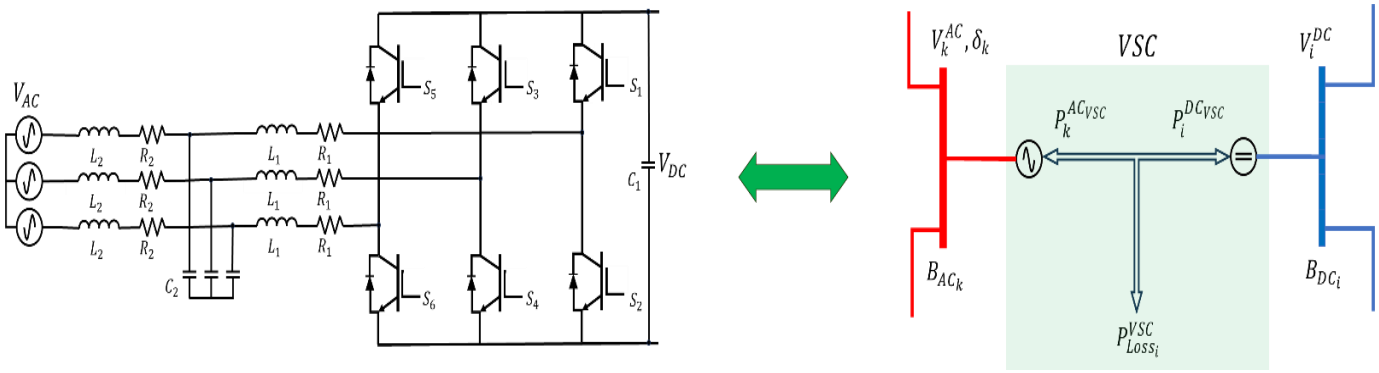

Figure 1. Equivalent VSC power flow model.

Figure 1 represents the simplified equivalent power flow model for the VSC. The variables on the AC side are associated with the voltage and phase at bus B_{AC_k} (V_k^{AC}, δ_k) and on the DC side associated with the voltage at bus B_{DC_i} (V_i^{DC}). The coupling for the AC/DC power flow is selected from the active power on the AC side ($P_k^{AC_{VSC}}$) and the active power on the DC side ($P_i^{DC_{VSC}}$), whose bidirectional power transfer presents losses ($P_{Loss_i}^{VSC}$) associated with the switching of the VSC IGBTs [23]. According to the equivalent model, the equations of power flow in the VSCs of the microgrid are established from (1), (2), and (3). These relate to the losses ($P_{Loss_i}^{VSC}$) as a quadratic function of the inverter current ($I_{Loss_i}^{VSC}$), which in turn depends on the active ($P_k^{AC_{VSC}}$) and reactive ($Q_k^{AC_{VSC}}$) power transfer of the VSC on the AC side. The coefficients a_i, b_i y c_i depend on the power and characteristics of the inverter.

$$P_k^{AC_{VSC}} + P_i^{DC_{VSC}} + P_{Loss_i}^{VSC} = 0 \tag{1}$$

$$I_{Loss_i}^{VSC} = \frac{\sqrt{{P_k^{AC_{VSC}}}^2 + {Q_k^{AC_{VSC}}}^2}}{V_k^{AC}} \tag{2}$$

$$P_{Loss_i}^{VSC} = a_i + b_i I_{Loss_i}^{VSC} + c_i {I_{Loss_i}^{VSC}}^2 \tag{3}$$

The apparent power rating ($S_k^{AC_{VSC_{max}}}$) limits the dispatch of active and reactive power in the VSC of the inverter on the AC side. The operating space of the inverter can be seen in a PQ plane representing the semicircle around the positive active power axis. The behavior of this semicircle is defined according to the operation of the VSC [24].

Figure 2a shows the operating region of the VSC coupled to the PVG in the PQ plane. This region is considered a minimum power factor (PF_{min}) value that sets the operational limit of the VSC. Thus, the reactive power ($Q_k^{AC_{VSC}}$) available for dispatch is restricted to the amount of active power ($P_k^{AC_{VSC}}$) available in the PVG based on a Maximum Power Point Tracking (MPPT) algorithm.

Figure 2b presents the zones of operation of the VSC associated with the BESS. In this one, an operation in the four quadrants of the PQ plane is observed since the BESS operates in charge ($P^{ESS}_{max_{Ch}}$) or discharge ($P^{ESS}_{max_{Dch}}$) mode limited by the maximum active power in the VSC and physical characteristics of the BESS. In both modes of operation, the BESS VSC can control the reactive power injection $Q^{AC_{VSC}}$.

According to the description of the operation of the VSCs coupled to the PVGs and BESS, the operational restrictions of the reactive power injection at all times t, limited by PF_{min} defined by the inverter characteristics, are defined as follows (4) y (5). The OPF algorithm adjusts the control variable $Q^{AC_{PVG}}_{k,t}$ and $Q^{AC_{ESS}}_{k,t}$ at each time instant according to the following operational constraints.

$$-tan\left(\theta^{AC_{PVG}}_{PF_{min}}\right)P^{AC_{PVG}}_{k,t} \leq Q^{AC_{PVG}}_{k,t} \leq tan\left(\theta^{AC_{PVG}}_{PF_{min}}\right)P^{AC_{PVG}}_{k,t} \quad (4)$$

$$-tan\left(\theta^{AC_{ESS}}_{PF_{min}}\right)P^{AC_{ESS_{max}}}_{k} \leq Q^{AC_{ESS}}_{k,t} \leq tan\left(\theta^{AC_{ESS}}_{PF_{min}}\right)P^{AC_{ESS_{max}}}_{k} \quad (5)$$

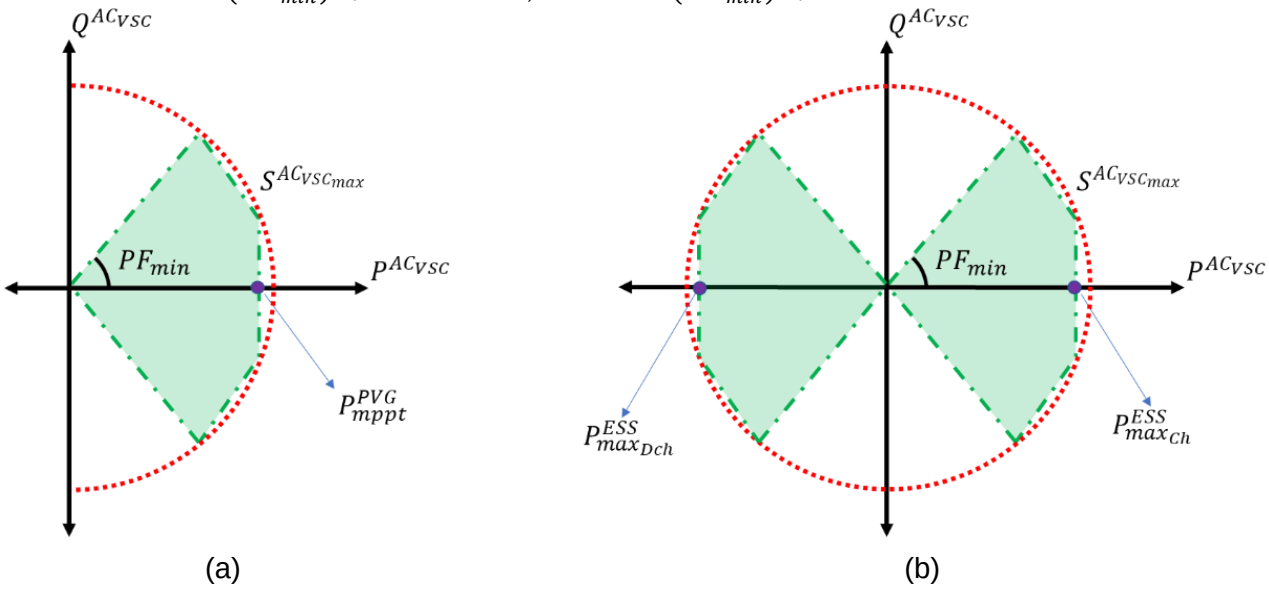

Figure 2. (a) Operating region of the VSC coupled to the PVG; (b) Operating region of the VSC coupled to the BESS.

Solar photovoltaic generation $\left(P^{XC_{PVG}}_{X,t}\right)$ is an exogenous variable that depends on environmental conditions such as irradiance and temperature. On the other hand, the energy available in the BESS depends on the operational requirements of the MHM, the optimal operating point set by the management algorithm, and the SoC of the BESS. The associated converters on the DC side control the active power $\left(P^{ESS_{DC}}_{i,t}\right)$ injected (battery discharge) or absorbed (battery charge) [25][26][27]. Similarly, on the AC side, the associated inverter allows the control of active and reactive power $\left(P^{ESS_{AC}}_{k,t}, Q^{ESS_{AC}}_{k,t}\right)$ independently, since the batteries are supplied with dispatchable energy, the available power is conditioned according to the SoC $\left(E^{AC_{ESS}}_{k,t}, E^{DC_{ESS}}_{i,t}\right)$ and the operating point of the MG [28]. The Multi-Period Optimal Power Flow (MPOPF) sets the load or discharge condition, equivalent to setting the power conditions at each instant during day-ahead optimal operation.

Lithium-ion batteries are used as a reference for power flow modeling in this work. A lithium-ion battery is the most recent technology, with a solid electrolyte, high energy density, and storage efficiency (η) higher than 90%, low self-discharge rates, and is not affected by memory effect [26]. In

(6) and (7) are presented the equations that model the SoC as a function of the power control variables, either as a battery charge or as a discharge on the AC side $\left(P^{AC_{ESS}}_{k,t} > 0, P^{AC_{ESS}}_{k,t} < 0\right)$ and the DC side $\left(P^{DC_{ESS}}_{i,t} > 0, P^{DC_{ESS}}_{i,t} < 0\right)$, respectively.

$$E^{AC_{ESS}}_{k,t} = E^{AC_{ESS}}_{k,t-1} + \eta P^{AC_{ESS}}_{k,t}\Delta t \quad (6)$$

$$E^{DC_{ESS}}_{i,t} = E^{DC_{ESS}}_{i,t-1} + \eta P^{DC_{ESS}}_{i,t}\Delta t \quad (7)$$

Smart Transformer-Enabled Meshed Hybrid Microgrids

The ST is a multi-stage power electronic converter with multiple Low Voltage (LV) and Medium Voltage (MV) ports, both AC and DC. The ST is more than a straightforward substitute for the conventional Low-Frequency Transformers (LFT) (60 Hz or 50 Hz). This device supplies many services to the intelligent electrical grid. It also eases the integration of new hybrid AC and DC microgrid architectures. Thus, the ST plays the role of an Energy router (ER) [29] since it can inject or absorb reactive power, mitigate harmonics [30], mitigate voltage sag [31], and limit current in the event of short-circuit faults [32]. In an ST-commanded grid, distributed resources are connected on the LV_{DC} side or the LV_{AC} side asynchronously with the grid side so that the low-voltage DC or AC frequency can be used as a feedback signal for power flow control. In this way, the power routing function is effectively achieved.

By taking advantage of the degrees of freedom offered by each stage of the multi-stage power electronic converter, the ST concept [33] was proposed, which provides DC connectivity [34] and reduces the reinforcement in the LV_{AC} distribution network caused by the increasing penetration of DER and BESS. The ST also represents a semi-decentralized solution for receiving network information since it functions as a controllable node to support the MV network [15]. The ST allows the formation of a hybrid meshed DS that provides voltage and power flow control to be achieved simultaneously with a centralized controller, as shown in Figure 3a. Under this scheme, a LV_{DC} is connected between the LV_{DC} ST link and the Distributed Generation Converters (DGC) at DC bus. This additional connection introduces several active power flow paths to support load demand. This new scheme reduces the complexity of the DGC control algorithms since the ST controls both LV_{AC} and LV_{DC} ports [14].

Figure 3b shows the structure of an ST with each control and communication layer. It is evident that the stages of the ST adapt a decoupled control structure, which allows power flow control independently and bidirectionally, thus obtaining a greater degree of freedom for power flow control in the AC and DC side.

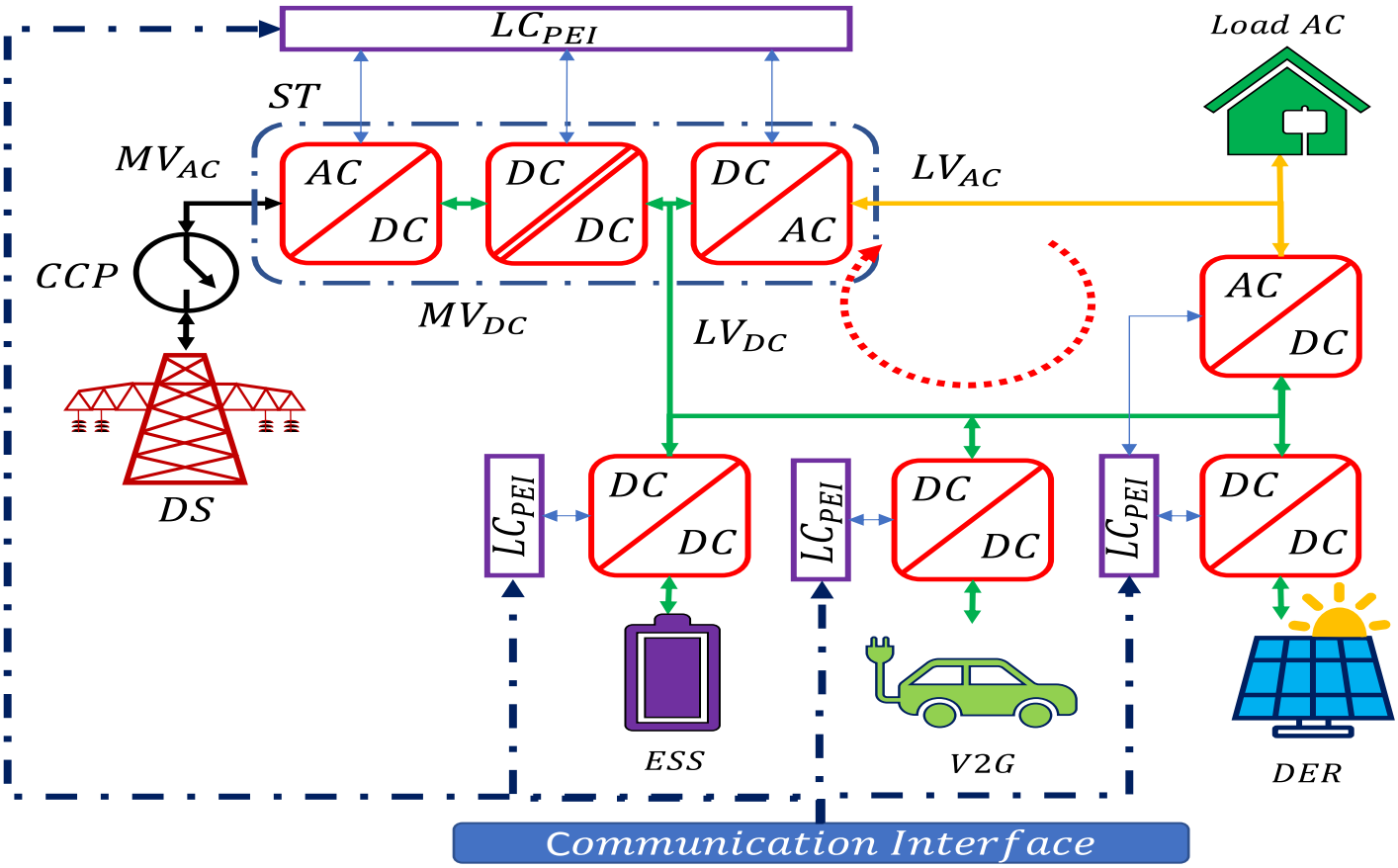

(a)

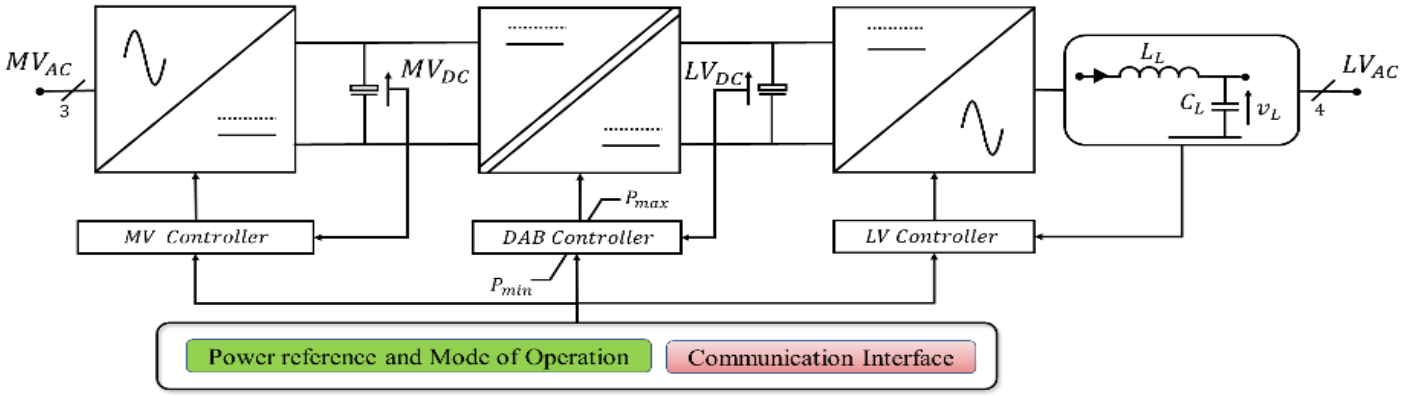

(b)

Figure 3. (a) Formation of a hybrid meshed DS; (b) The basic structure of a three-stage ST

For power flow analysis in the MHM, the second stage output of the ST is modeled as a controlled DC feeder (G_{DC_i}), which allows active ($P_{k,t}^{AC_{VSC}}$) and reactive ($Q_{k,t}^{AC_{VSC}}$) power injection on the AC side or active power ($P_{i,t}^{DC_{VSC}}$) on the DC side compactly and flexibly, so we would have an active inverter in the system; this stage also allows us to regulate the voltage level on the DC side. Thus, the conventional VSC is replaced by an active VSC for control and injection of active and reactive power according to the criteria and control variables provided by the optimization mechanism. So, a DC generator is introduced in the load flow equations associated with the DC side. The equivalent model for power flow studies at the AC and DC coupling ports of the ST are presented in Figure 4, and the power flow equations are described by (8), (9) for the AC side, and (10) for the DC side.

$$P_{k,t}^{G_{AC}} + P_{k,t}^{AC_{ST}} - P_{k,t}^{L_{AC}} - P_{k,t}(V,\delta) = 0 \tag{8}$$

$$Q_{k,t}^{G_{AC}} + Q_{k,t}^{AC_{ST}} - Q_{k,t}^{L_{AC}} - Q_{k,t}(V,\delta) = 0 \tag{9}$$

$$P_{i,t}^{G_{DC}} + P_{i,t}^{DC_{ST}} - P_{i,t}^{L_{DC}} - P_{i,t}^{DC}(V) = 0 \tag{10}$$

In (11), it describes the objective function: cost of energy exchange of the microgrid with the DS ($f_{c,t}$), the losses in the lines ($f_{l,t}$) and the voltage deviation in the AC and DC side $\left(f_{dV_{AC,t}} + f_{dV_{DC,t}}\right)$ at all times t. $f_{c,t}$ is given by (12), it relates to the operating cost $\left(c_k^{AC}, c_i^{DC}\right)$ to the feeder power $\left(P_{k,t}^{G_{AC}}, P_{i,t}^{G_{DC}}\right)$ on the AC and DC side, respectively. $f_{l,t}$ is given by (13), which establishes the relationship between generation, either feeder $\left(P_{k,t}^{G_{AC}}, P_{i,t}^{G_{DC}}\right)$ of the DS or PVG $\left(P_{k,t}^{PV_{AC}}, P_{i,t}^{PV_{DC}}\right)$, and demand $\left(P_{k,t}^{L_{AC}}, P_{i,t}^{L_{DC}}\right)$, including the charging or discharging mode of the BESS $\left(P_{k,t}^{ESS_{AC}}, P_{i,t}^{ESS_{DC}}\right)$. Finally, the voltage deviation on both the AC and DC sides is given by (14) and (15).

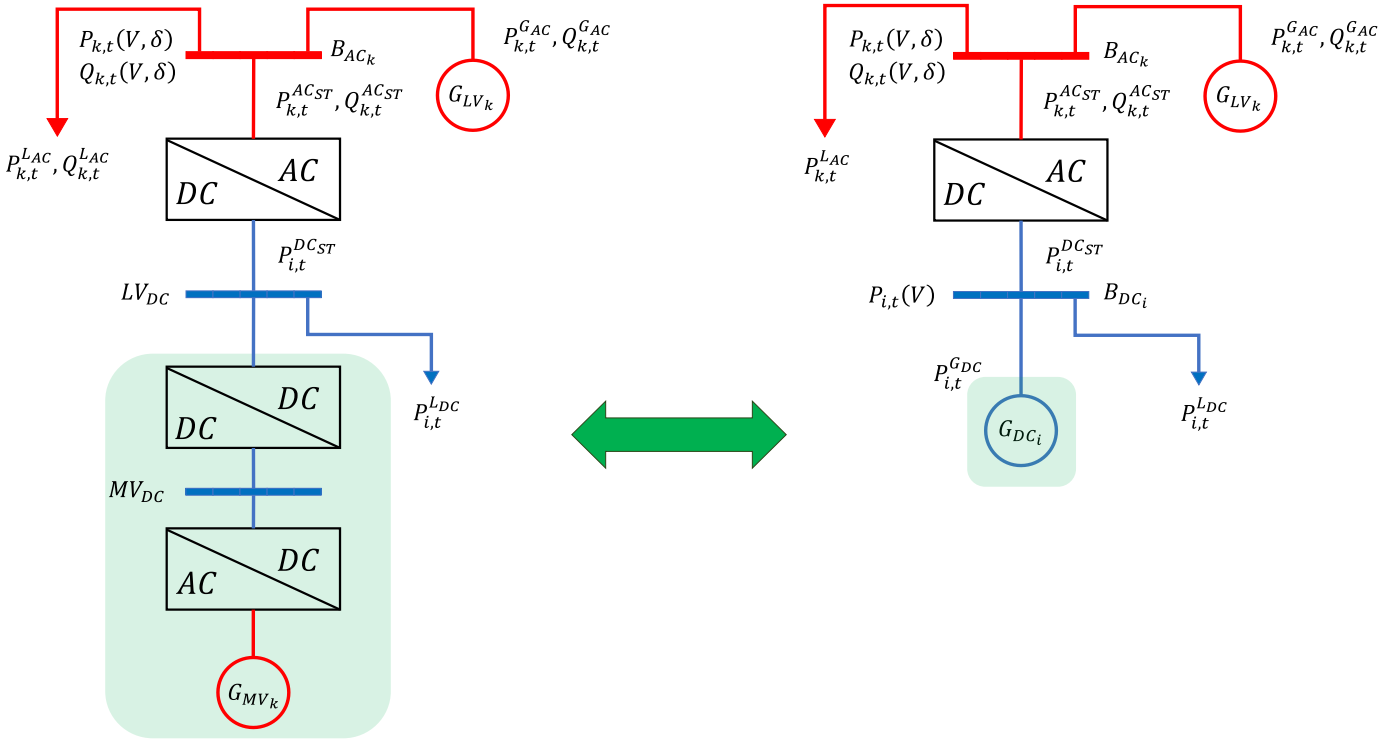

Figure 4. Equivalent ST power flow model.

$$min \sum_{t=0}^{T} \left(w_c f_{c,t} + w_l f_{l,t} + w_d \left(f_{dV_{AC,t}} + f_{dV_{DC,t}} \right) \right) \tag{11}$$

$$c_k^{AC} \sum_{k=0}^{N^{G_{AC}}} P_{k,t}^{G_{AC}} + c_i^{DC} \sum_{i=0}^{N^{G_{DC}}} P_{i,t}^{G_{DC}} \tag{12}$$

$$\sum_{k=0}^{N^{G_{AC}}} P_{k,t}^{G_{AC}} + \sum_{i=0}^{N^{G_{DC}}} P_{i,t}^{G_{DC}} + \sum_{k=0}^{N^{PVG_{AC}}} P_{k,t}^{PV_{AC}} + \sum_{i=0}^{N^{PVG_{DC}}} P_{i,t}^{PV_{DC}} - \sum_{k=0}^{N^{ESS_{AC}}} P_{k,t}^{ESS_{AC}} - \sum_{i=0}^{N^{ESS_{DC}}} P_{i,t}^{ESS_{DC}} - \sum_{k=0}^{N^{L_{AC}}} P_{k,t}^{L_{AC}} - \sum_{i=0}^{N^{L_{DC}}} P_{i,t}^{L_{DC}} \tag{13}$$

$$\sum_{k=0}^{N^{AC}} \left(V_{k,t}^{AC} - 1.0 \right)^2 \tag{14}$$

$$\sum_{i=0}^{N^{DC}} \left(V_{i,t}^{DC} - 1.0 \right)^2 \tag{15}$$

The optimization problem is subject to the combination constraints from (1) to (10), including the operational limits of the feeders, voltages, and maximum power transfer on both AC and DC lines. The complete power balance constraints on the AC and DC side are given by (16), (17), and (18), respectively.

$$P_{k,t}^{G_{AC}} + P_{k,t}^{PV_{AC}} + P_{k,t}^{AC_{VSC}} - P_{k,t}^{ESS_{AC}} - P_{k,t}^{L_{AC}} - P_{k,t}(V,\delta) = 0 \tag{16}$$

$$Q_{k,t}^{G_{AC}} + Q_{k,t}^{PV_{AC}} + Q_{k,t}^{AC_{VSC}} - Q_{k,t}^{ESS_{AC}} - Q_{k,t}^{L_{AC}} - Q_{k,t}(V,\delta) = 0 \tag{17}$$

$$P_{i,t}^{G_{DC}} + P_{i,t}^{PV_{DC}} + P_{i,t}^{DC_{VSC}} - P_{i,t}^{ESS_{DC}} - P_{i,t}^{L_{DC}} - P_{i,t}^{DC}(V) = 0 \tag{18}$$

Benchmark Test-System

Analysis cases were proposed to address the AC-DC optimization problem, taking the benchmark reported in (36) as a reference. It takes the parameters of the lines, loads, and busbar connections of the North American configuration low voltage distribution system. It has a radial structure starting at the secondary of a medium- to low-voltage transformer, MV of 12.47 kV and LV of 208 V, for each sub-network. The LV lines are either subway, mainly in urban areas with high load density, or overhead, mainly in rural areas with comparatively low load density. A one-line equivalent modified MHM schematic of the interconnection of the LV commercial sub-networks is shown in Figure 5.

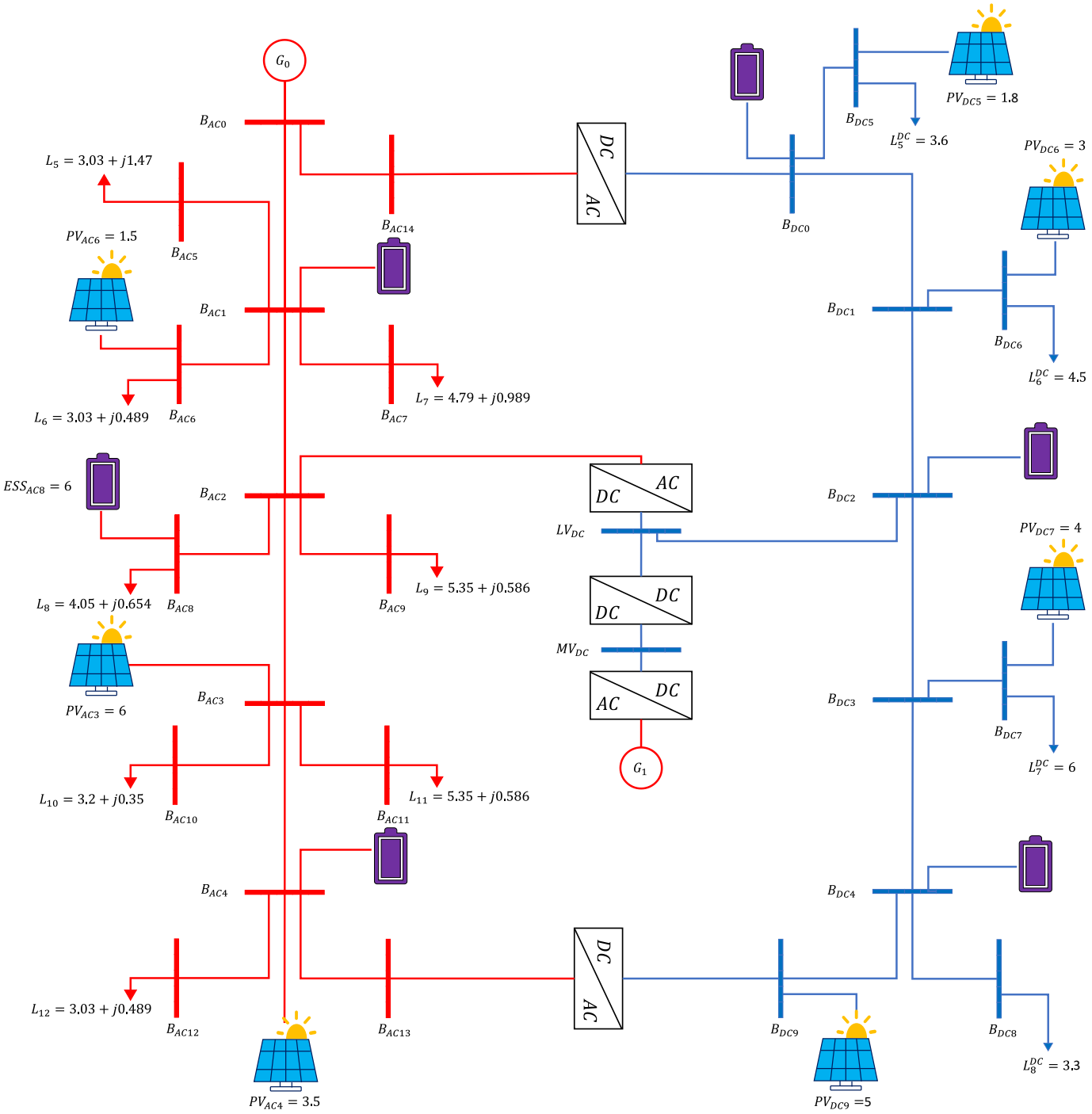

Figure 5. Benchmark Test-System ST-based MHM.

The MG in Figure 5 consists of 15 AC busbars - 11 DC busbars. It has a feeder connected to B_{AC0}, which corresponds to the low voltage output of the transformer secondary at the common coupling point. The

coupling of the 15 AC busbars with the 11 DC busbars is made from tow VSC coupled between B_{AC14} and bus B_{DC0}, bus B_{AC13} and bus B_{DC9}, and finally, the ST is connected to bus B_{AC2} and bus B_{DC10}. PVG of 11 kW on the AC side and 13.8 kW on the DC side is integrated. As a base case, this equates to approximately 50% of the demand, considered a system with medium DG penetration [26]. Likewise, BESS is introduced on both the AC and DC sides coupled to their respective PEI with a capacity of 120 kWh. The connection of the PVG and BESS is distributed according to Figure 5. It should be noted that the MHM features a second 12.47 kV MV feeder connected at the first stage of the ST. This constitutes a DC equivalent feeder under the principle of operation of the ST described in the previous section.

The PVGs are placed in the bars where critical loads are considered (B_{AC6}, B_{DC5}, B_{DC6}, and B_{DC7}) and coupling points of load distribution branches as well as in the outer part of the feeder, which is susceptible to presenting a greater voltage deviation (B_{AC3} and B_{AC4}, and B_{DC9}).

The BESS allows the storage of surplus energy during a time slot to be used later in a different time slot when there is a higher demand that coincides with periods of low generation in the PVGs. Similarly, the BESS allows reactive power control on the AC side from the optimal management of the PEI coupled to each storage system. According to the power flow equations, the BESS supplies power in the MG, discharge condition for negative power. In case of positive power, the BESS is charging. For both scenarios, charging and discharging, reactive power control is performed according to the optimal operation requirements of the MG in each time slot.

BESSs are connected to the system at points where additional services are required to support active and reactive power injection. On the AC side BESS are connected to buses B_{AC1}, B_{AC4}, and B_{AC8}, thus presenting a mechanism to support reactive power injection and energy storage for optimal use during periods of low PVG and high demand. Under this same approach, BESS are connected on the DC side on buses B_{DC0}, B_{DC2}, and B_{DC4}, with a storage capacity close to 60 kW-h.

RESULTS

This section presents the results of the computational model proposed, which intends to evaluate the behavior of the ST-based MHM under different levels of penetration of distributed energy resources based on a multi-objective multi-period problem to minimize operating cost, voltage deviation, and losses in AC/DC microgrid and VSC's power dispatch.

The multi-objective multi-period power-optimal optimization problem was programmed in Python 3.9.5 language in the Spyder 5.4.2 integrated development environment under the Pyomo 6.5.0 framework. Also, the *Ipopt* solver was used to treat nonlinear problems.

Four case studies are proposed to validate the impact of DER in MG and determine the performance of the MHM management algorithm, in which two levels of PVG penetration (medium and high) are presented in two groups of MGs, one where only the VSCs are introduced at each coupling point between the AC and DC side of the MG; and another group in which the ST is presented as a power router whose equivalent model is proposed as a DC controllable feeder.

- Case I: A VSC-based MHM with close to 50% PVG penetration level is considered.
- Case II: An ST-based MHM with close to 50% PVG penetration level is considered.
- Case III: A VSC-based MHM with close to 80% PVG penetration level is considered.
- Case IV: An ST-based MHM with close to 80% PVG penetration level is considered.

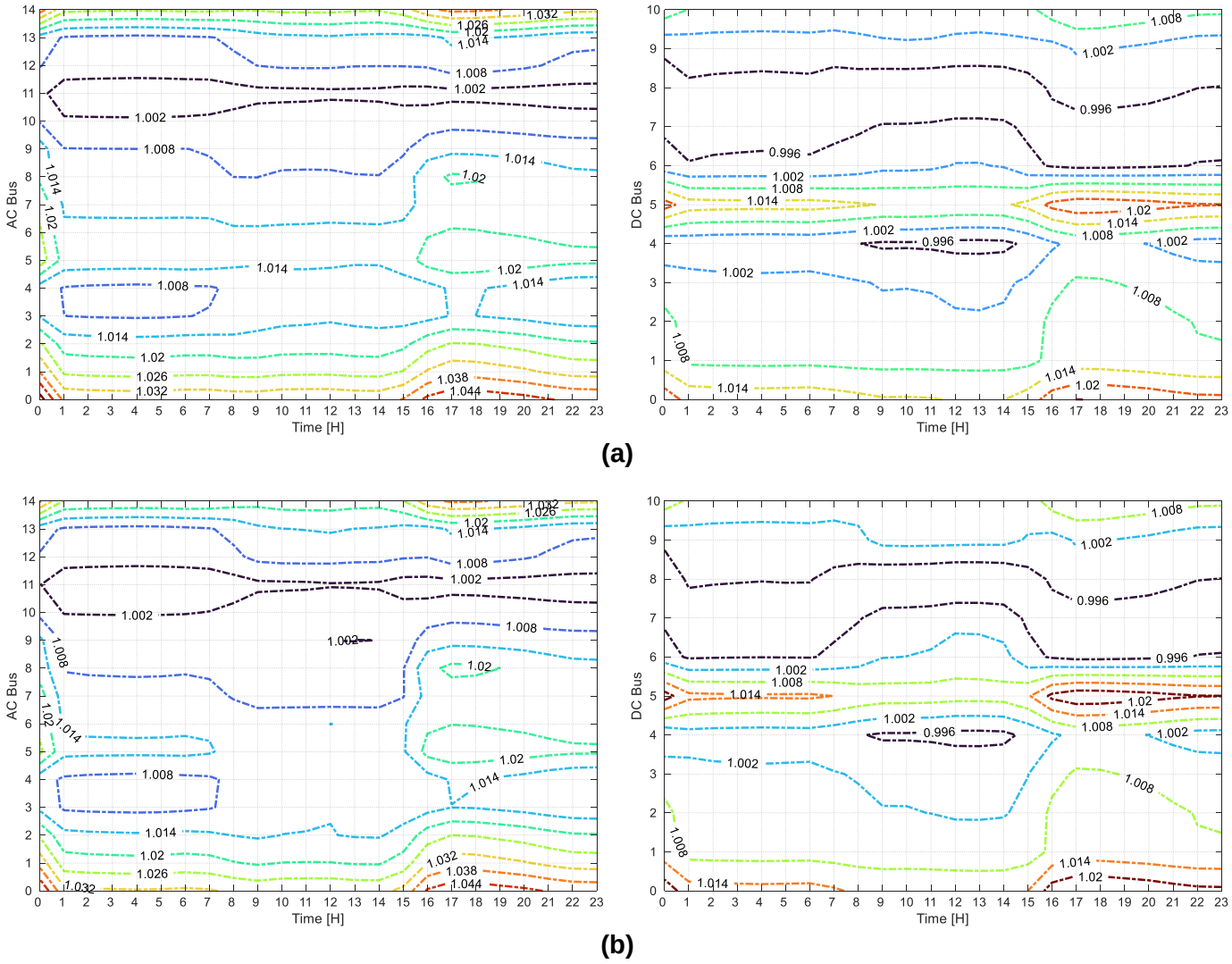

Figure 6. (a) Case I: Voltage profiles on the AC and DC side; (b) Case II: Voltage profiles on the AC and DC side

For each case, we seek to establish the decision variables of the problem associated with the voltage deviation in the system, the operational cost of the MHM, and the related losses according to the operating conditions of each case study. Likewise, the control variables associated with set points of each VSC and ST and the PEI coupled to the PVG and BESS for the control of active and reactive power are determined.

Given that we seek to determine the impact of the penetration of the DER on the MHM and the impact of the ST on the management of the MHM, cases I and II, as well as cases III and IV, are directly compared. For cases I and III, the MG in Figure 5 is modified by replacing the ST with a VSC connecting bus B_{AC2} to bus B_{DC10} (LV_{DC}). Case II and IV present the same configuration as Figure 5. PVG is added on both the AC and DC sides of the MG. For cases I and II, on the AC side, it has a penetration close to 22%, while on the DC side, it presents a penetration close to 27% for an overall penetration in MHM growing to 50%. For cases III and IV, on the AC side, it has a penetration close to 48%, while on the DC side, it presents a penetration close to 31% for an overall penetration in MHM growing to 80%.

Figure 6 shows the voltage profiles of the B_{AC14} on the AC side and the B_{DC10} on the DC side for Cases I and II. In Case I, the feeder connected to the AC side regulates the voltage with a reference of 1 p.u. ($S_{Base} = 50\,kW, V_{AC\,Base} = 120\,V$), on the farthest buses from an increase in the voltage on bus B_{AC0}. However, the DERs contribute to compensating the voltage on the rest of the buses connected in the MG branches, given the power injected into the system in a distributed manner. On the DC side, the VSC connected to DC B_{DC10} regulates the voltage with a reference of 1 p.u. ($S_{Base} = 50\,kW, V_{DC\,Base} = 500\,V$). An overvoltage is observed on B_{DC5} due to the power injection of the DERs on that bus (20 kWh from BESS and 1.8 kW from PVG), as well as on B_{DC0} (DC side from VSC), there is an overvoltage due to it being connected to the DC port of the VSC connected to the AC bus closest to the feeder on the AC side. This phenomenon occurs mainly between 15:00 and 23:00 hours.

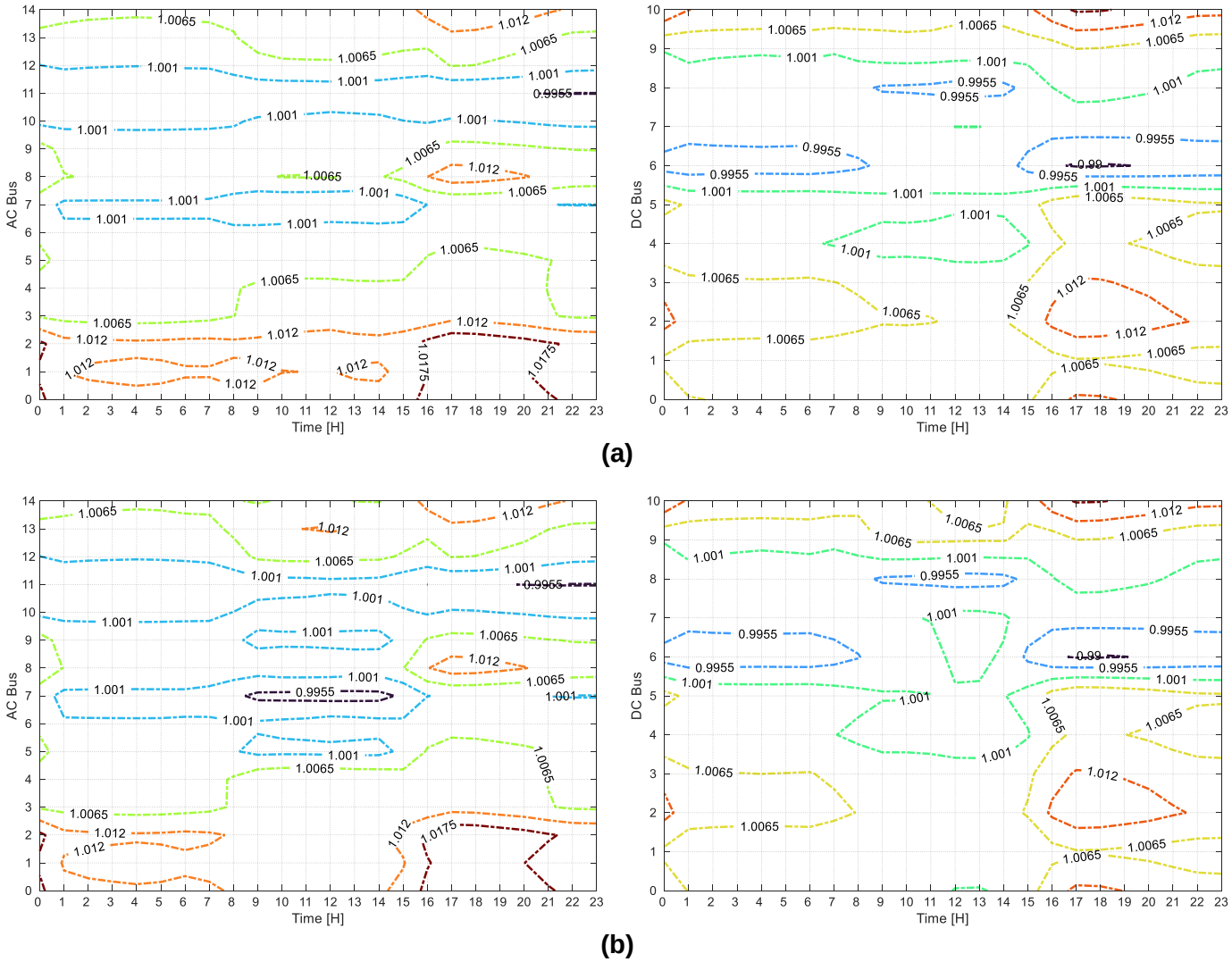

Figure 7. (a) Case III: Voltage profiles on the AC and DC side; (b) Case IV: Voltage profiles on the AC and DC side

In Case II, there is a reduction in the voltage deviation on both AC and DC sides. This is evidenced by a more uniform color distribution and closeness to the reference color range at 1 p.u. The ST allows voltage compensation by integrating a second feeder in the MHM. It is observed that in the central buses of the MHM, the voltage profile is close to the reference value. However, during peak demand, an overvoltage is kept in the buses closer to the system's AC generator, and the MHM's voltage profile is better achieved. On the bus B_{AC2} corresponding to the low voltage AC port of the ST, a reduction in voltage deviation is shown since a controlled and bidirectional transfer of power between the DC and AC side of the system is performed; a similar profile is maintained on the DC port of the ST connected to the bus B_{DC10}. In both Case I and Case II, the voltage profiles where the coupling VSCs are associated between the AC and DC side maintain a similar voltage deviation profile since the VSCs do not have an active power transfer control, unlike in the ST.

Figure 7 shows the voltage profiles for Cases III and IV. As in Cases I and II, the AC side power supply regulates the voltage with a reference of 1 p.u. on the farthest buses from an increase in the voltage on bus B_{AC0}, although with an increase of close to 1.01 p.u. In Case IV, including the ST contributes to voltage regulation in both the AC and the DC side. On the other hand, since there is a higher PVG penetration in the MHM, a lower voltage deviation is observed in all AC and DC buses during the 24 hours; despite this, in Case III, there is an increase in voltage in B_{AC0} and B_{AC2} between 16:00 and 20:00 hours. The high penetration DERs contribute to compensating the voltage on the buses connected in the MG branches. The tension presents a better profile on the DC side, evidenced by a better color distribution close to 1 p.u. In Case III, there are areas with a considerable deviation between 15:00 and 20:00 hours, both on the AC and DC sides, on buses B_{AC0}, B_{AC1}, and B_{AC14}, and B_{DC0}, B_{DC1}, and B_{DC10}. This phenomenon occurs mainly between 15:00 and 23:00 hours.

Despite having a high DER penetration, a better voltage profile is presented. The ST allows voltage compensation by integrating a second feeder in the MHM and power flow control between the AC and DC

sides. It is observed that in the central buses of the MHM (B_{AC2} and B_{DC10}), the voltage profile is close to the reference value and does not exceed 1.01 p.u. However, during peak demand, an overvoltage is kept in the buses closer to the system's AC generator, and the MHM's voltage profile is better achieved. On the AC bus, B_{AC2} corresponding to the low voltage AC port of the ST, a reduction in voltage deviation is shown since a controlled and bidirectional transfer of power between the DC and AC side of the system is performed; a similar profile is maintained on the DC port of the ST connected to the B_{DC10}.

Figure 8 shows the active and reactive power injected by the PVGs for Cases I and II (a), as well as Cases III and IV (b), in which, according to the availability of solar resources and the needs of the MG in each hourly interval, the operating point of the PEI is adjusted to control the reactive power injection dynamically, controlled by the minimum power factor (PF), set at 0.85, either in backward or forward. The time slot with the highest power injection is between 6 and 17:00 hours.

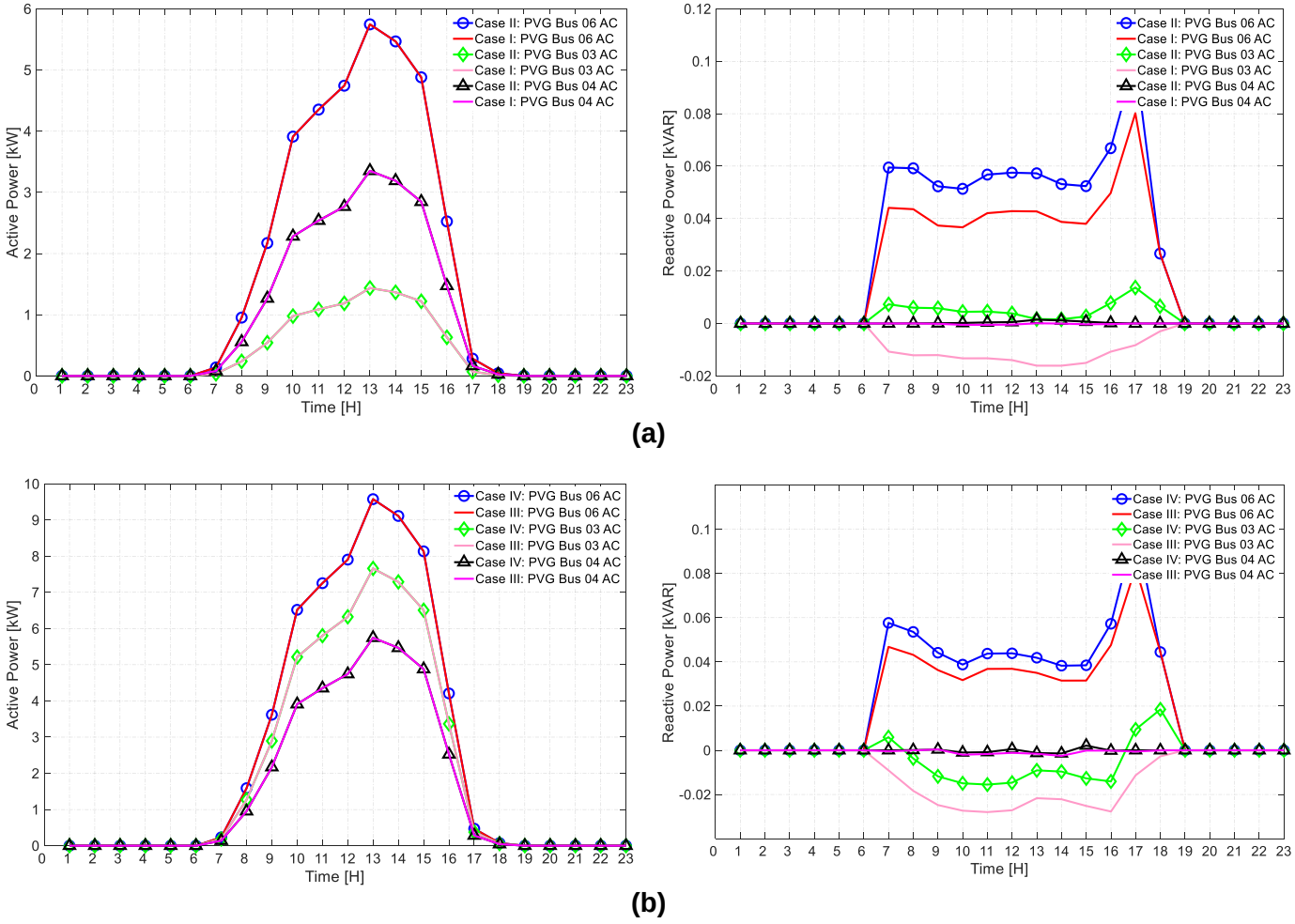

Figure 8. (a) Active power injected by the PVGs on the AC side; (b) Reactive power injected by the PVGs on the AC side.

Comparing Case I with Case II, the reactive power in the PVG connected to B_{AC3} is set as support for voltage regulation in this bus. In Case I, a forward PF power is injected. In contrast, a backward PF power is injected in Case II, given the effect of both active and reactive power control, which allows ST implementation in Case II. On the other hand, the PVG connected to B_{AC4} presents a value very close to zero since the reactive power support, according to the MG operating conditions, is supplied from the energy available in the BESS connected to B_{AC4}; this happens in both cases. Finally, a forward PF power is injected from the PVG connected to B_{AC6} to meet the reactive power demand in the load connected to this bus. It also supports the load requirements on B_{AC7} and the needs of the other AC system buses further away from the B_{AC0} feeder. In this way, active power support is evidenced mainly to meet the demand and reactive power due to the need for voltage regulation in some areas of the network. Still, the functionality in the PEI is used for reactive power control to meet the demand and voltage regulation in the far buses of the AC feeder, and this is also in line with the need to minimize voltage deviation in the network, mainly in the distant parts of the feeders with the highest peak demand. On the other hand, on the DC side, the generation profiles are like those

presented in Figure 8 but are assorted according to the peak power of the PVG installed in each DC bus. In this case, only active power control is performed, which mainly seeks to meet the demand according to the availability of the energy resource.

In Cases III and IV, there is a reduction in the amount of power injected into the grid. This is related to the penetration level in these case studies. Despite this, it is observed that around 17:00 hours, a peak close to 0.1 kVAR is followed, like what happens in Cases I and II, given that around that time slot, there is a peak demand in the MHM, leading to an increase in voltage deviation, as shown in Figures 6 and Figure 7, which is compensated with the injection of reactive power into the system. On the other hand, a slight increase in reactive power injection with a forward PF is observed in B_{AC3}.

Figure 8 shows the effect of high PVG penetration on the MHM. For a 50% PVG penetration, there is an increase in reactive power injection to compensate for the demand needs and support voltage regulation. On the other hand, by increasing PVG penetration by 80%, it is observed that there is a reduction in the reactive power injected since the availability of active power increases the voltage in some areas of the MHM. The amount of reactive power to the grid is reduced to reduce this voltage increase. For these two scenarios, it is evident that the ST allows better power control management since a minimum reactive power injection is always maintained concerning the management carried out in the MHM only with VSC.

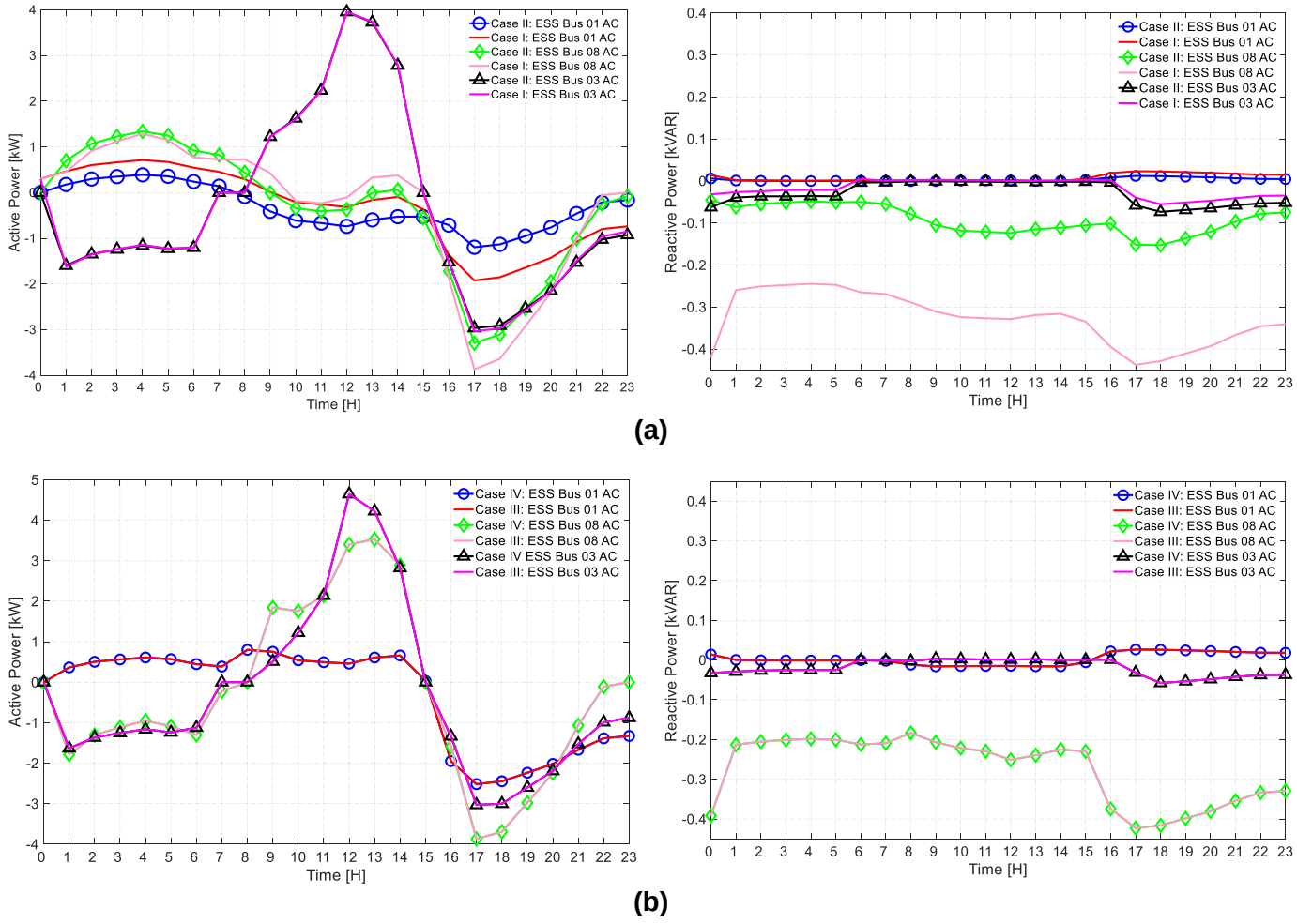

Figure 9. (a) Active power injected by the BESS on the AC side; (b) Reactive power injected by the BESS on the AC side.

Figure 9 shows the BESS charging and discharging patterns (a) and the reactive power injection (b) from the PEI control coupled to each BESS on the AC side. From 0:00 to 8:00 hours, the BESS connected to buses B_{AC1} and B_{AC2} are charging, while the BESS connected to B_{AC4} is discharged, mainly in Cases I and II, although there is a reduction in the rate of charge in Case II. During that same time slot, the BESS connected on B_{AC4} present a rate of energy discharge to support the needs of the network. Between 9:00 and 14:00 hours, an opposite effect occurs, in which the BESSs connected to B_{AC4} are charged, and the other BESSs are discharged. During the period of peak demand, between 15:00 and 23:00 hours, all BESSs are discharged. A similar charging and discharging profile are maintained on B_{AC4} in both cases. In the other

buses, the improvement in the charging and discharging profile of the BESS is observed by integrating the ST for power control in the MHM.

During daily operation, power injection with a leading power factor is observed regarding reactive power. This is evidence of the functionality of the BESS to compensate for the voltage deviation, mainly in B_{AC8} Case I is a phenomenon that coincides with the voltage profiles in Figure 6a. The other BESSs have a lower power injection since it is supported from different points of the MHM; these two conditions are related to the fact that the PVGs keep part of the demand, and the surplus energy is stored. For 24 hours, the BESS connected to B_{AC8} of Case I injects reactive power into the MG, which supports the compensation of the MG since B_{AC8} is a central bus that derives a large part of the MG demand on the AC side.

Case I and IV loading and unloading patterns are like Cases I and II. However, given that there is an 80% increase in the PVG penetration level, it is observed that the BESS patterns of B_{AC1} both cases (III and IV) are maintained in load conditions between 0:00 and 08:00 hours, while the other BESSs are maintained in unloaded conditions to support the demand and other services required by the MHM during this period. During peak PVG generation, both BESSs remain in load condition, taking advantage of the available resources. In Cases III and IV, since there is a more significant energy resource available in the DERs, most of the time, all the BESSs are in the same operating condition (charging or discharging), the effect of which is to have greater energy availability during the period of peak demand. As for reactive power, it's observed in advance during the 24 hours; however, the effort between 00:00 and 15:00 hours is lower than in Cases I and II, increasing from 16:00 hours to compensate for the voltage deviation during peak demand in the MHM. In all cases, it is observed that the availability of the solar resource and the possibility of storing it for later use during demand peaks are better exploited by incorporating the ST for optimal management of the MHM since this device offers additional degrees of freedom to the optimization algorithm to better set the operating point of the PEI in the MHM.

Figure 10 shows the SoC in 24 hours of operation of the BESSs in Case I and II (a) and Case III and IV (b). The BESS connected to B_{AC4} presents a gmore significant deviation in the state of charge, mainly because they are connected to the most extreme buses of the MHM, thus requiring a gmore excellent compensation of available active and reactive power. On the other hand, the BESS systems connected on B_{AC1} and B_{AC8} are fully charged during the middle of the period of maximum generation in the PVGs to support the peak demand represented after 15:00 hours. A similar phenomenon occurs in the BESSs on Case III and IV, which are loaded during part of the day to support the MHM's requirements during peak demand.

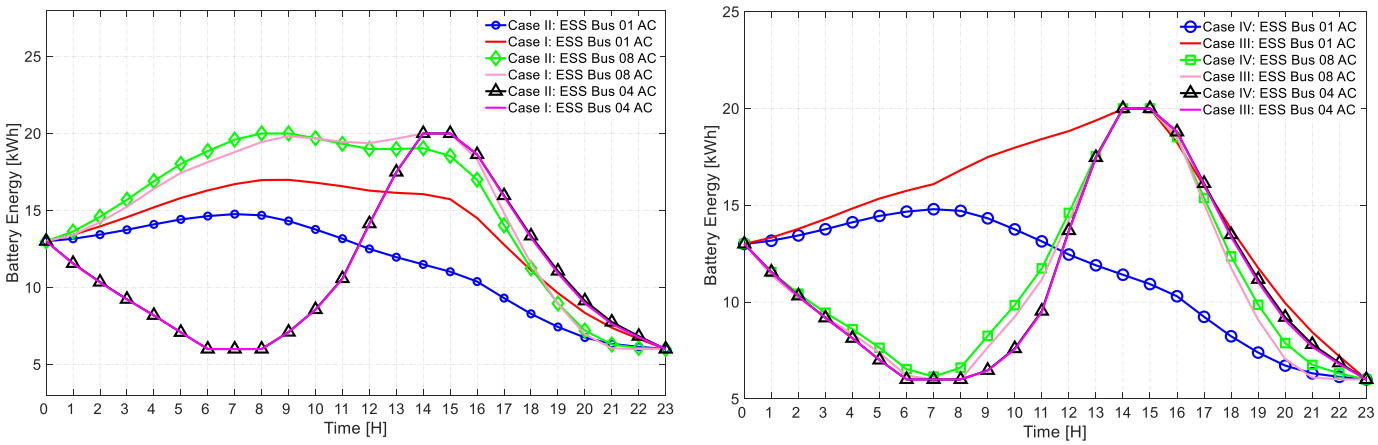

(a) **(b)**

Figure 10. (a) Active power is injected by the BESS on the AC side; (b) Reactive power is injected by the BESS on the AC side.

It should be noted that the BESSs start with a SoC close to 70%. It is observed that the BESS has a depth of discharge close to 30%. Accordingly, the BESS connected to B_{AC4} presents a complete discharge between 6:00 and 8:00 hours, becoming harmful and affecting the useful life of the BESS. Likewise, it is observed that the BESS is fully charged between 14:00 and 15:00 hours, a time that coincides with the end of the period of maximum generation in the PVG. Case III shows how the SoC conditions of the BESSs are altered in the VSC-based MHM, while in the ST-based MHM, it is observed that despite operating with a penetration close to 80%, SoC profiles like Case II are maintained, thus proving the impact of managing the MHM from an ST under different levels of PVG penetration.

Figure 11 shows the charging and discharging profile of the BESS on the DC side. The bidirectional DC-DC converters allow controlling the charging and discharging conditions in each time slot according to the MG requirements and the optimal solution set by the EMS in each operating hour. During peak generation in the PVGs (between 10:00 and 15:00 hours), the BESSs present a load power transfer above 1 kW. In contrast, in the periods of minimum generation, the BESSs serve the demand, mainly in the slot between 15:00 and 23:00 hours, taking advantage of the energy stored during the maximum generation of the DERs of the MHM. This phenomenon is similar for all cases, whose main difference is observed in the power transfer rates, either charging or discharging, given that, with a higher level of PVG penetration, there is a greater availability of stored energy, which allows a more excellent power transfer according to the SoC of the BESS and the needs of the MHM. Under these operating conditions, the connected BESSs of Case II and IV show a reduction in SoC relative to Cases I and III, despite the increased level of PVG penetration in each case. The performance of BESS in VSC-based MHMs presents a more significant variation between the minimum and maximum value of the SoC. This situation affects the performance and degradation of the BESS under real operating conditions. The reduction in SoC variation in the BESS connected in ST-based MHMs is compensated by a better redistribution of power transfer conditioned by SoC in the other BESSs located in different points of the MHM, given the control of active power transfer between the AC and DC side of the MHM, as well as the availability of the resource, which, when efficiently managed, allows improving the overall performance of the MHM.

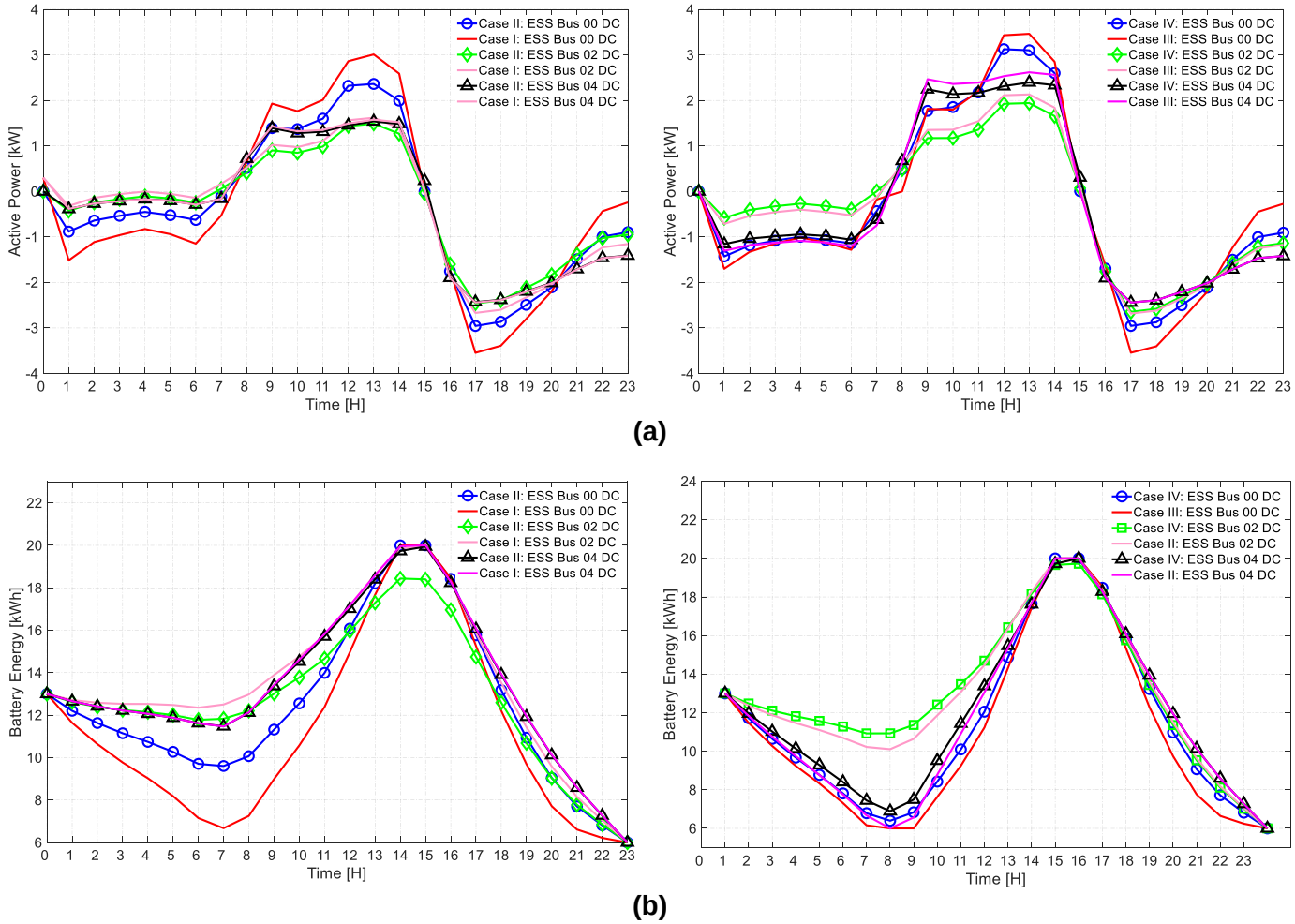

Figure 11. (a) Active power injected by the BESS on the DC side; (b) Total energy of the BESS on the DC side.

Another aspect closely related to the variables analyzed above and showing the impact of the ST in the MHM is the power transfer between the AC and DC sides of the MHM. The active power transfer is directly related to the operating point of the MG, both on the AC and DC side, as presented in (1). The reactive power is controlled independently by the operating point set by the management system, which respects the constraints associated with the nominal apparent power of each converter. Thus, Figure 12 shows the transfer of active and reactive power in the VSCs according to the operating conditions of each case under study.

Based on the data visualized in Figure 12, it is observed that the third stage of the ST is working in rectifier mode, so that it channels power from the AC side to the DC side, which is transferred to DC MG and the AC side, again, through the VSCs of B_{AC13} and B_{AC14}, which works in inverter mode, to ensure the power balance of the MHM. In Cases III and IV, it is observed that the transfer of active power is reduced since there is greater availability of solar photovoltaic resources that are used to cover the demand of the network and, at the same time, stored for later use in peak demand periods. It should be noted that the greatest power transfer is made in the third station of the ST, which reduces the effort of the other converters of the MHM.

Regarding reactive power, it is observed that in Case III and IV, a greater reactive power injection with PF, both in forward and backward, since there is a greater PVG penetration, tends to increase the voltage deviation so that, to compensate for it, reactive power must be injected in the MHM, in addition to the support provided by the reactive power control in the PEI and VSC. B_{AC2} presents the highest reactive power transfer in the MHM. However, the ST allows optimized management in reactive power injection by achieving better performance of the MHM under minimum reactive injection. During the peak load period, the highest injection of active and reactive power is observed concerning what happens with voltage profiles, PVG generation profiles, and energy stored in the BESS.

Table 1 presents a comparison of the optimal solution of the decision variables of the MPOPF problem. The four scenarios analyzed are compared, thus comparing the optimal value of each objective function. For the cost of energy exchange of the microgrid with the DS ($f_{c,t}$), the losses in the lines ($f_{l,t}$) and the voltage deviation in the AC and DC side $\left(f_{dV_{AC,t}} + f_{dV_{DC,t}}\right)$ at all times t, are compared in the ache case study.

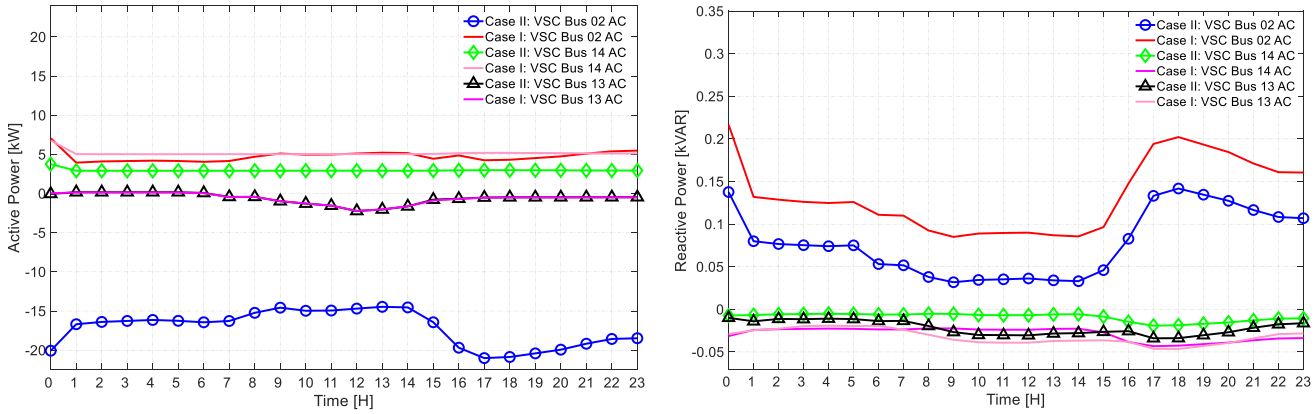

(a)

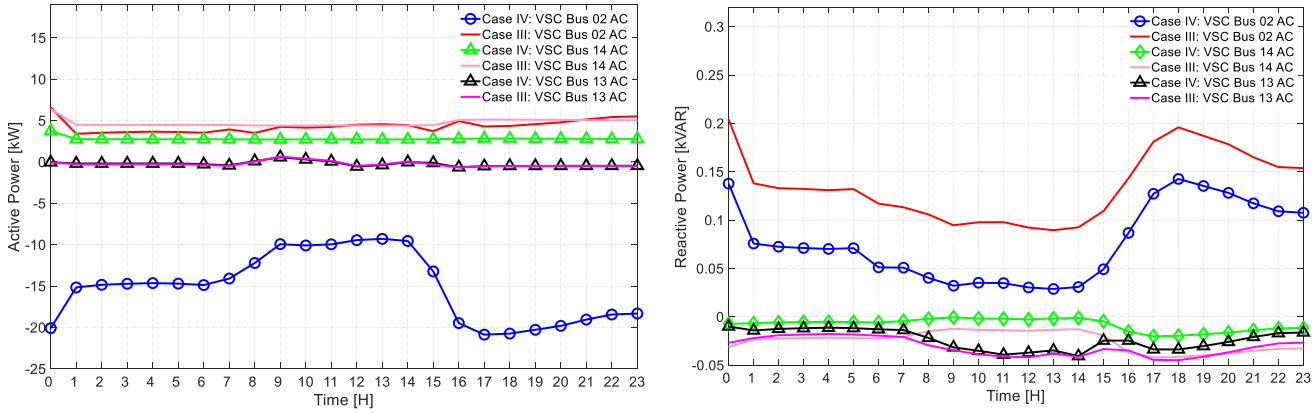

(b)

Figure 12. (a) The VSC transferred active and Reactive power in Cases I and II; (b) Active and Reactive power was transferred by the VSC in Cases III and IV.

Table 1. Comparative Case Study

Objective Function	Case I	Case II	Case III	Case IV
Cost of energy exchange [$/kW]	22.94	22.54	20.22	19.94
Losses in the lines [kW]	23.00	11.44	20.32	10.96
AC Voltage deviation [V^2]	0.12	0.02	0.10	0.02
DC Voltage deviation [V^2]	0.02	0.01	0.02	0.01

Table 1 shows that in the cases where an MHM structure based on ST presents a reduction in losses close to 50% for the losses recorded in the MHM based on VSC. As for voltage deviation, a decrease of about 84% is observed on the AC side, and on the DC side, a reduction of about 50 % in all cases. Although the cost of energy exchange with the DS has slight variations in each case, it should be added that in Cases II and IV, there is an additional cost for the energy exchange in the feeder on the DC side. This implies that the cost of the AC feeder is reduced in each case and on the DC side since the increased PVG penetration reduces the energy exchange with the DS and consequently reduces the overall operating cost of the MHM.

In Cases II and IV, the impact of adding the ST was observed, even though this introduced an additional operating cost on the DC side. For these cases, under medium and high PVG penetration conditions, the management system manages to minimize the control and decision variables of the optimization problem in higher proportion compared to the results achieved with the VSC-based MHMs in Cases II and III. The ST allows the addition of a new controllable feeder on the DC side; this significantly impacts loss reduction since integrating this into a flail structure enables better power transfer paths. The flail structure was implemented based on VSCs, but by combining them with the ST, the overall performance of the MHM was optimized in terms of voltage deviation and loss reduction under different operating scenarios.

The optimal solution from the formulation of an MPOPF problem to minimize operating cost, voltage deviation, and losses in MHM, which was found given the degrees of freedom provided by the Power dispatch in Voltage-Sourced Converters associated with photovoltaic generators, energy storage systems, and ST, facilitate the control of active power transfer between the AC and DC side of the MHM, as well as the management of power transfer between the MHM and the BESS. Similarly, these devices allow independent control of reactive power at different points of the MHM, facilitating voltage regulation maneuvers according to peak demand and optimization objectives that improve performance in the daily operation of the MHM.

CONCLUSION

The results show the positive impact of Smart Transformer-based Meshed Hybrid Microgrids with high and medium penetration of distributed energy resources, main PVG, is evident. Since there are energy storage and power control systems in the different MHM buses, it was possible to take better advantage of the functionalities of the ST as an energy router.

Formulating a multi-period problem allowed us to minimize operating costs, voltage deviation, and losses in MHM, increasing the efficiency and performance of BESS, VSC, and ST functionalities. It also allowed the simultaneous control of active and reactive power to meet the load requirements, voltage regulation, and loss reduction.

An Optimal Power Dispatch in Voltage-Sourced Converters associated with photovoltaic generators, energy storage systems, and ST management systems was developed, which allowed the control of active power transfer between the AC and DC sides, the control of active power injected in the MHM and the optimization of the SoC of the BESS as well as the optimization of reactive power injection to reduce voltage deviation during peak demand periods.

Funding: This work was partially supported by the Science, Technology, and Innovation Fund of the General System of Royalties under the Excellence Scholarship Program 2019 - Ministry of Science, Technology, and Research – *Minciencias* Colombia.
Conflicts of Interest: The authors declare no conflict of interest.

REFERENCES

1. Judge MA, Khan A, Manzoor A, Khattak HA. Overview of smart grid implementation: Frameworks, impact, performance and challenges. J Energy Storage [Internet]. 2022 May;49:104056. Available from: https://linkinghub.elsevier.com/retrieve/pii/S2352152X22000950

2. Badal FR, Sarker SK, Nayem Z, Moyeen SI, Das SK. Microgrid to smart grid's evolution: Technical challenges, current solutions, and future scopes. Energy Sci Eng [Internet]. 2022 Oct 19; Available from: https://onlinelibrary.wiley.com/doi/10.1002/ese3.1319
3. Viola J, Aceros C. Smart Grids and their Applicability for the Development of the Electricity Sector for Colombia in the year 2050. In: IOP Conference Series: Materials Science and Engineering [Internet]. Institute of Physics Publishing; 2016 [cited 2020 Oct 17]. Available from: https://app.dimensions.ai/details/publication/pub.1059177154?search_mode=content&search_text=%22Colombia%22 AND %22distributed generation%22&search_type=kws&search_field=full_search&or_facet_year=2016&or_facet_year=2017&or_facet_year=2018&or_facet_year=20
4. Chicco G, Ciocia A, Colella P, Di Leo P, Mazza A, Musumeci S, et al. Introduction—Advances and Challenges in Active Distribution Systems. In: Lecture Notes in Electrical Engineering [Internet]. Springer Science and Business Media Deutschland GmbH; 2022 [cited 2022 Nov 21]. p. 1–42. Available from: https://link.springer.com/chapter/10.1007/978-3-030-90812-6_1
5. Sahoo SK, Sinha AK, Kishore NK. Control Techniques in AC, DC, and Hybrid AC-DC Microgrid: A Review. IEEE J Emerg Sel Top Power Electron. 2018 Jun 1;6(2):738–59.
6. Unamuno E, Barrena JA. Hybrid ac/dc microgrids - Part I: Review and classification of topologies. Renew Sustain Energy Rev [Internet]. 2015;52:1251–9. Available from: http://dx.doi.org/10.1016/j.rser.2015.07.194
7. Al-Ismail FS. DC Microgrid Planning, Operation, and Control: A Comprehensive Review. IEEE Access. 2021;9:36154–72.
8. Planas E, Andreu J, Gárate JI, Martínez De Alegría I, Ibarra E. AC and DC technology in microgrids: A review. Renew Sustain Energy Rev. 2015;43:726–49.
9. Jia L, Zhu Y, Wang Y. Architecture design for new AC-DC hybrid micro-grid. In: 2015 IEEE 1st International Conference on Direct Current Microgrids, ICDCM 2015 [Internet]. IEEE; 2015 [cited 2021 Mar 3]. p. 113–8. Available from: https://ieeexplore.ieee.org/document/7152020/
10. Li Y, Sun Q, Dong T, Zhang Z. Energy management strategy of AC/DC hybrid microgrid based on power electronic transformer. Proc 13th IEEE Conf Ind Electron Appl ICIEA 2018. 2018;2677–82.
11. Garcés-Ruiz A. Small-signal stability analysis of dc microgrids considering electric vehicles. Rev Fac Ing. 2018;(89):52–8.
12. Zhu R, Liserre M, Langwasser M, Kumar C. Operation and Control of Smart Transformer in Meshed and Hybrid Grids. IEEE Ind Electron Mag [Internet]. 2020 [cited 2021 Mar 3];15:43–57. Available from: https://ieeexplore.ieee.org/document/9305209/
13. Kumar C, Gao X, Liserre M. Smart Transformer Based Loop Power Controller in Radial Power Distribution Grid. Proc - 2018 IEEE PES Innov Smart Grid Technol Conf Eur ISGT-Europe 2018.
14. Nour M, Chaves-Ávila JP, Magdy G, Sánchez-Miralles Á. Review of Positive and Negative Impacts of Electric Vehicles Charging on Electric Power Systems. Energies [Internet]. 2020 Sep 8 [cited 2021 Mar 3];13(18):4675. Available from: https://www.mdpi.com/1996-1073/13/18/4675
15. Das D, Hrishikesan VM, Kumar C, Liserre M. Smart Transformer-Enabled Meshed Hybrid Distribution Grid. IEEE Trans Ind Electron [Internet]. 2021 Jan 1 [cited 2021 Mar 3];68(1):282–92. Available from: https://ieeexplore.ieee.org/document/8960525/
16. Zhu R, De Carne G, Andresen M, Liserre M. Control of Smart Transformer in Different Electric Grid Configurations. ICPE 2019 - ECCE Asia - 10th Int Conf Power Electron - ECCE Asia. 2019;3:1668–75.
17. Gupta A, Doolla S, Chatterjee K. Hybrid AC-DC Microgrid: Systematic Evaluation of Control Strategies. IEEE Trans Smart Grid. 2018;9(4):3830–43.
18. Zhu R, Liserre M. Operation and supervision control in smart transformer-based meshed and hybrid grids. In: 6th IEEE International Energy Conference, ENERGYCon 2020 [Internet]. IEEE; 2020 [cited 2021 Mar 3]. p. 1019–23. Available from: https://ieeexplore.ieee.org/document/9236572/
19. Das D, Hrishikesan VM, Kumar C. BESS-PV Integrated Islanded Operation of ST-based Meshed Hybrid Microgrid. 2020 IEEE 9th Int Power Electron Motion Control Conf IPEMC 2020 ECCE Asia. 2020;(Ccm):2122–8.
20. Hrishikesan VM, Kumar C. Operation of Meshed Hybrid Microgrid During Adverse Grid Conditions with Storage Integrated Smart Transformer. IEEE Open J Ind Electron Soc [Internet]. 2021;2:315–25. Available from: https://ieeexplore.ieee.org/document/9404809/
21. Hrishikesan VM, Kumar C. Smart Transformer Based Meshed Hybrid Microgrid with MVDC Interconnection. In: IECON Proceedings (Industrial Electronics Conference) [Internet]. IEEE; 2020 [cited 2021 Mar 3]. p. 4961–6. Available from: https://ieeexplore.ieee.org/document/9255284/
22. Meng L, Sanseverino ER, Luna A, Dragicevic T, Vasquez JC, Guerrero JM. Microgrid supervisory controllers and energy management systems: A literature review. Renew Sustain Energy Rev [Internet]. 2016 Jul;60:1263–73. Available from: https://linkinghub.elsevier.com/retrieve/pii/S1364032116002380
23. De Aquino CCCB, Blasi TM, Unsihuay-Vila C, Fernandes TSP, Pinto RS, de Lara Filho MO, et al. A Hierarchical Framework for Day-Ahead Optimal Operation Planning of Active Distribution Networks with Multi-Microgrids. Brazilian Arch Biol Technol [Internet]. 2023;66. Available from: http://www.scielo.br/scielo.php?script=sci_arttext&pid=S1516-89132023000100615&tlng=en

24. Zhao Q, García-González J, Gomis-Bellmunt O, Prieto-Araujo E, Echavarren FM. Impact of converter losses on the optimal power flow solution of hybrid networks based on VSC-MTDC. Electr Power Syst Res. 2017;151(September 2017):395–403.
25. Lachovicz FJ, Fernandes TSP, Vilela Junior JA. Impacts of PV-STATCOM Reactive Power Dispatch in the Allocation of Capacitors Bank and Voltage Regulators on Active Distribution Networks. J Control Autom Electr Syst [Internet]. 2023 Aug 4;34(4):796–807. Available from: https://link.springer.com/10.1007/s40313-023-00995-6
26. González-Castellanos A, Pozo D, Bischi A. Distribution System Operation with Energy Storage and Renewable Generation Uncertainty. In: Resener M, Rebennack S, Pardalos PM, Haffner S, editors. Handbook of Optimization in Electric Power Distribution Systems [Internet]. Cham: Springer International Publishing; 2020. p. 69–120. (Energy Systems). Available from: http://link.springer.com/10.1007/978-3-030-36115-0
27. Blasi, Thaís Marzalek. Planning of active distribution systems operations with batteries and renewable energy sources [Internet]. Curitiba; 2019 [cited 2023 Apr 14]. Available from: https://acervodigital.ufpr.br/handle/1884/67163
28. Oliveira GA. Programação diária da operação de redes ativas de distribuição considerando a inserção de veículos elétricos [Internet]. Curitiba; 2019. Available from: https://acervodigital.ufpr.br/handle/1884/65647
29. Lachovicz FJ. Planejamento de suporte de reativo para redes de distribuição com forte penetração de geração solar fotovoltaica. 2018.
30. Huang AQ. 2 - Solid state transformers, the Energy Router and the Energy Internet. In: Su W, Huang AQBT-TEI, editors. Woodhead Publishing; 2019. p. 21–44. Available from: http://www.sciencedirect.com/science/article/pii/B9780081022078000023
31. Syed I, Khadkikar V, Zeineldin HH. Loss Reduction in Radial Distribution Networks Using a Solid-State Transformer. IEEE Trans Ind Appl. 2018 Sep 1;54(5):5474–82.
32. Jeyapradha RB, Rajini V. Investigations on Service Extensions of Solid State Transformer. In: 5th International Conference on Electrical Energy Systems, ICEES 2019. Institute of Electrical and Electronics Engineers Inc.; 2019.
33. Jakka VN, Acharya S, Anurag A, Prabowo Y, Kumar A, Parashar S, et al. Protection design considerations of a 10 kV SiC MOSFET enabled mobile utilities support equipment based solid state transformer (muse-SST). In: Proceedings: IECON 2018 - 44th Annual Conference of the IEEE Industrial Electronics Society. Institute of Electrical and Electronics Engineers Inc.; 2018. p. 5559–65.
34. Zhu R, Andresen M, Langwasser M, Liserre M, Lopes JP, Moreira C, et al. Smart transformer/large flexible transformer. CES Trans Electr Mach Syst. 2021;4(4):264–74.
35. Zhu R, Buticchi G, Liserre M. Investigation on Common-Mode Voltage Suppression in Smart Transformer-Fed Distributed Hybrid Grids. IEEE Trans Power Electron. 2018;33(10):8438–48.
36. Strunz K, Abbey C, Andrieu C, Campbell RC, Fletcher R. Benchmark Systems for Network Integration of Renewable and Distributed Energy Resources - TF C6.04.02. CIGRE Task Force C6.04.02. 2014.